Materials Today Communications 51 (2026) 114752

Contents lists available at ScienceDirect

Materials Today Communications

journal homepage: www.elsevier.com/locate/mtcomm

CFD and experimental investigation of channel diameter effects in structured internally cooled grinding wheels

Sharlane Costa [a,b,c], Paulina Capela [a,b,d], Maria Sousa [e], Amauri Hassui [f], João Ribeiro [c,*], Mário Pereira [g], Delfim Soares [a,b]

[a] CMEMS - Center for MicroElectromechanical, University of Minho, Guimarães 4800-058, Portugal
[b] LABBELS – Associate Laboratory, Braga, Guimarães, Portugal
[c] Centro de Investigação de Montanha (CIMO), Instituto Politécnico de Bragança, Campus S. Apolónia, Bragança 5300-253, Portugal
[d] MEtRICs, Mechanical Eng. Dep., Univ. of Minho, Campus de Azurém, Guimarães, Portugal
[e] Univ. of Minho, Campus de Azurém, Guimarães, Portugal
[f] Department of Manufacturing and Materials Engineering, School of Mechanical Engineering, University of Campinas – UNICAMP, Campinas, São Paulo 13083-860, Brazil
[g] Centro de Física das Universidades do Minho e do Porto, Braga, Portugal

ARTICLE INFO

Keywords:
Grinding performance
Internal cooling system
Structured grinding wheel
Computational fluid dynamics (CFD)
Sustainable manufacturing

ABSTRACT

Efficient cooling and lubrication are critical in grinding due to the high specific energy and limited contact area involved. Conventional external methods often fail to penetrate the air barrier formed by the rotating wheel, leading to excessive heat generation and reduced process stability. To overcome this limitation, this study investigates vitrified alumina grinding wheels with internal cooling channels designed for directed fluid delivery. Three structured configurations were developed, all with identical total outlet area (~54 mm²) but different channel diameters (0.6, 1.0, and 1.5 mm), to isolate the effect of channel size on fluid flow and grinding behavior. Computational fluid dynamics (CFD) simulations were performed to assess outlet velocity and surface coverage, while grinding tests quantified tangential and normal forces, temperature variation (ΔT), force ratio (F_t/F_n), and specific grinding energy. Narrow channels provided uniform surface coverage but limited jet velocity due to higher hydraulic resistance, whereas wider channels enhanced outlet velocity at the expense of flow uniformity. The intermediate configuration (Ø 1.0 mm) yielded the most balanced performance, achieving up to 38 % lower tangential force and 41 % lower temperature than the Ø 0.6 mm design, while maintaining low specific energy across all depths of cut. Correlation between CFD and experimental results confirmed that both jet intensity and spatial distribution govern cooling and lubrication efficiency. These insights support the design of more efficient and sustainable grinding wheels through tailored channel geometries.

1. Introduction

Grinding is a process widely used in finishing operations due to its ability to generate surfaces with high geometric and dimensional quality [1]. However, it is an operation characterized by intense heat generation [2,3], resulting from the high specific energy of the process and the reduced contact area between tool and workpiece [4,5]. The main mechanisms responsible for this heat include grain–workpiece friction, plastic deformation of the surface layer, and grain fracture. Friction at the abrasive–workpiece interface converts most of the mechanical energy directly into heat. Plastic deformation of the workpiece material further increases temperature through internal energy dissipation within the subsurface layer, while grain fracture and bond fracture release additional heat by absorbing part of the mechanical energy during chip formation. The combined action of these effects leads to thermal accumulation in the grinding zone [6–9]. This accumulated heat can compromise surface integrity, induce residual stresses, microcracks, and microstructural changes in the workpiece [10–12]. To mitigate such effects, large volumes of lubricating–cooling fluid are commonly applied, which in turn lead to a series of operational challenges [13,14].

The presence of an air barrier adhered to the surface of the grinding wheel at high rotation speeds hinders the effective penetration of the fluid into the cutting zone, often requiring even higher flow rates to compensate for this effect [15,16]. It is estimated that more than 4

* Corresponding author.
E-mail addresses: scosta@dem.uminho.pt (S. Costa), jribeiro@ipb.pt (J. Ribeiro).

https://doi.org/10.1016/j.mtcomm.2026.114752
Received 9 October 2025; Received in revised form 14 December 2025; Accepted 28 January 2026
Available online 29 January 2026

million tons of cutting fluids are consumed annually worldwide, most of them based on petroleum-derived mineral oils [17]. This massive consumption not only generates high costs, accounting for up to 15–17 % of total production costs and three to five times the cost of the tools themselves, but also poses serious environmental risks. Just one liter of mineral oil can contaminate up to one million liters of water, compromising aquatic ecosystems and soil fertility [18].

In addition to the environmental impact, cutting fluids poses significant occupational health risks. Exposure can occur through inhalation of mists, dermal contact, or accidental ingestion of contaminated particles, and has been associated with chronic respiratory problems, dermatological disorders, and even potential carcinogenic effects [19–22].

From a broader sustainability perspective, both the life cycle of grinding wheels and the excessive use of coolants are increasingly critical. To address these concerns, several alternative strategies have been proposed, such as MQL, cryogenic cooling, and textured grinding wheels [23,24]. Although these strategies have shown partial improvements, they present inherent limitations. Minimum quantity lubrication (MQL) provides limited cooling capacity in high-energy grinding, which restricts its applicability [25,26]. Cryogenic cooling offers effective heat dissipation but lacks adequate lubrication and requires costly infrastructure, reducing its industrial feasibility [27,28].

Among these, surface texturing of grinding wheels has been widely investigated as a means to improve coolant accessibility and facilitate chip evacuation [29,30]. Recent studies have demonstrated the potential of this approach in reducing grinding temperature, controlling tool wear, and improving surface quality [31–34]. However, as the wheel wears, all these surface-based solutions gradually lose their effectiveness.

A more robust alternative is the integration of internal cooling channels, capable of delivering fluid directly from the wheel center to the contact zone, thereby overcoming the air barrier generated by rotation and maintaining efficiency throughout the entire wheel life [35–37]. Among the earliest and most systematic investigations in the field of internal cooling channels were those of Sieniawski and co-workers. In their study, vitrified alumina wheels with 1, 2 or 3 rows of radial channels demonstrated that even with a 90 % reduction in fluid flow (0.5 vs. 5.0 L/min), the process remained thermally stable, surface quality comparable to flood was preserved [38], and grinding forces were 20–25 % lower, with a slower force increase over time suggesting longer wheel life [39].

The main limitation, however, lies in the manufacturing method. Patent PL203295B1 [40] describes the formation of channels by means of tensioned metallic wires inserted through the mold during pressing, which are later removed mechanically to leave continuous channels. Any geometric modification requires a new mold, making the process inflexible. Moreover, the resulting channels are always linear, preventing the creation of curved, interconnected, or non-circular structures.

More recently, other authors have explored internal cooling channels using additive manufacturing, such as Barmouz et al. (2023) [41] who produced resin-bonded wheels with cylindrical and venturi-shaped channels. The fluid was supplied externally through customized holders and guided into the internal channels, with results showing substantial reductions in grinding forces, improved tool life, and higher G-ratio, especially for venturi configurations. Nevertheless, despite the promising results, the Digital Light Processing (DLP) approach remains more suited for prototyping and resin-bonded wheels of limited size, since the long curing times per layer make the process difficult to apply at industrial scale. In addition, because coolant is still supplied externally, a large amount of fluid is wasted and only a small fraction actually enters the slots, as evidenced by the high flow rates required in their tests (45 L/min).

This transition from surface-based to internally cooled designs represents the logical evolution of fluid delivery systems in grinding, combining enhanced lubrication efficiency with longer tool durability. The design of internal coolant systems has evolved toward increasingly complex geometries. Early approaches were restricted to simple radial holes [42], while more recent studies explored multi-layer arrangements [38,39,43], additive manufacturing of venturi-shaped channels [41], and surface slot textures [44]. Despite these advances, most solutions remain limited either by manufacturing constraints or by continued reliance on external flooding.

The performance of internal lubrication strongly depends on the geometry of the channels, in particular their diameter, quantity and distribution along the grinding wheel surface [43]. It is therefore essential to investigate how these parameters influence the outlet velocity, fluid distribution, and the ability to effectively reach the grinding zone. Furthermore, the definition of optimal channel geometry involves complex trade-offs: while narrow channels promote wide surface coverage, they also increase pressure losses; larger channels offer greater jet momentum but reduce coverage, leading to possible zones of insufficient lubrication.

The application of computational simulations, especially computational fluid dynamics (CFD), has proven to be a valuable tool for understanding this surface behavior of flow in structured wheels [45–50]. Through this approach, it is possible to visualize the trajectory of the jets at the outlets of the channels, estimate the distribution of velocities over the surface of the wheel and identify coverage patterns and areas of possible inefficiency [51]. Furthermore, simulation allows comparing different geometries without the need for multiple experimental steps, contributing to a more rational and efficient design of channels [49]. However, studies that integrate CFD modeling with experimental validation in real cutting conditions are still limited in the literature for structured grinding wheels with radial internal channels applied to surface grinding.

In this context, the present work investigates the influence of channel diameter in structured vitrified wheels with internal lubrication for surface grinding. The study specifically addresses the lack of research isolating the diameter effect under a constant outlet area and combining CFD and experimental analysis. Three vitrified wheels with internal channels of different diameters (0.6, 1.0, and 1.5 mm) were designed and manufactured via the sacrificial PLA insert method, all maintaining a total outlet area of approximately 54 mm^2 to ensure fair comparison. The analysis integrates CFD simulations to characterize outlet profiles and fluid distribution, with experimental tests assessing thermal and tribological performance. The results clarify the relationship between channel geometry and lubrication effectiveness, supporting the optimized design of structured grinding wheels with internal cooling.

2. Materials and methods

2.1. Production of structured wheels

Three structured abrasive grinding wheels with internal channels were developed for this study. The manufacturing process followed the conventional route for vitrified grinding wheels, with the addition of a specific step: the incorporation of polymeric structures made of polylactic acid (PLA), responsible for forming the internal channels [52]. These structures were previously modeled in CAD software and fabricated by additive manufacturing, creating a radial network as illustrated in Fig. 1a–c. The PLA structures were positioned inside the mold, together with the mixture of abrasive grains (alumina, 220 mesh) and vitrified bond, and the assembly was then compacted with a defined pressure cycle.

Subsequently, the green bodies were subjected to the standard sintering cycle. During this process, the PLA was fully decomposed, creating continuous hollow channels, as shown in Fig. 1d–f. This method allowed the formation of well-defined channels without compromising the structural integrity of the tool. The final bulk density of the vitrified wheel was 2.14 g/cm^3 . Additional details about the process are available in Costa et al. (2024) [52].

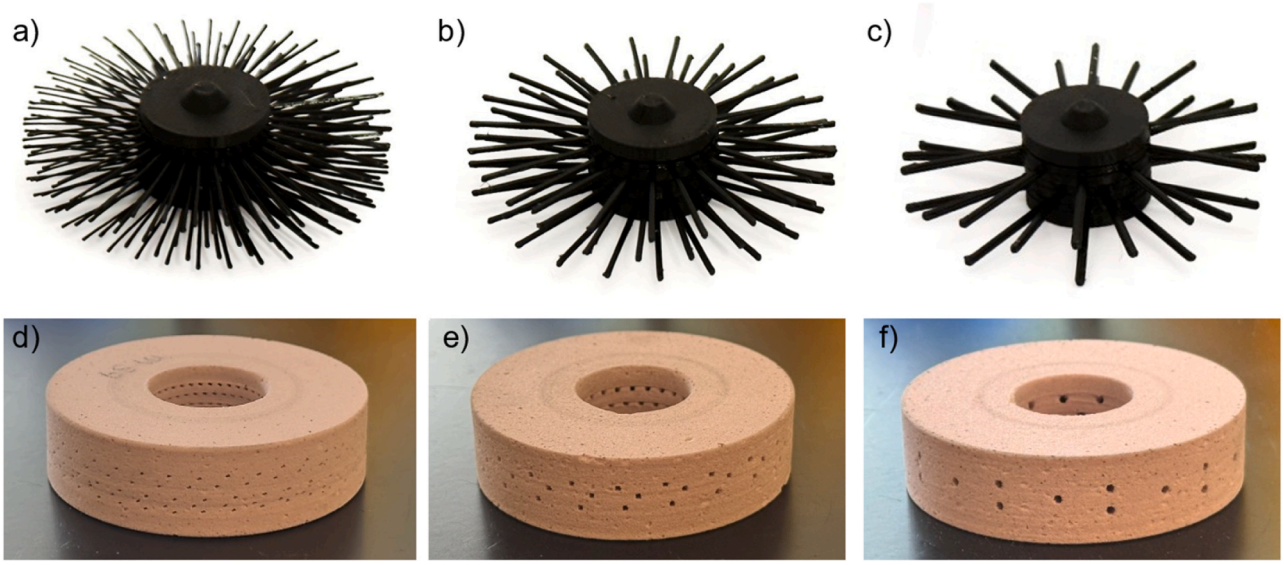

Fig. 1. Internal 3D structures, in PLA (a–c) and corresponding sintered grinding wheels (d–f) with different channel configurations: (a, d) 190 channels of ø 0.6 mm; (b, e) 69 channels of ø 1.0 mm; (c, f) 30 channels of ø 1.5 mm.

All grinding wheels were designed with identical external dimensions (62 mm in diameter, 15 mm in width, and 21 mm in inner diameter), differing only in their internal channel configurations. The design strategy was based on two main principles. First, the total outlet area was fixed at approximately 54 mm^2 to provide a normalized baseline and eliminate bias related to different flow capacities. This approach ensures that any observed differences in fluid distribution or cooling efficiency arise solely from the channel diameter. Second, the selected diameters (0.6, 1.0, and 1.5 mm) were chosen to cover the most relevant range for vitrified wheels with internal lubrication, combining manufacturing feasibility and distinct hydraulic behaviors. Diameters below 0.6 mm approach the lower limit of the sacrificial-insert technique, where channels may deform or close during sintering, while diameters above 1.5 mm tend to produce more concentrated outlet jets and larger interruptions on the cutting surface, potentially affecting the local contact conditions. Thus, this range represents a practical balance between fluid coverage, outlet velocity, and structural integrity.

The number of layers and interlayer spacing were derived from the wheel geometry and from structural feasibility considerations. Configurations with 3 or 5 layers were adopted to ensure a sufficiently uniform radial distribution of outlets without excessively reducing the abrasive volume or compromising wheel strength. The corresponding axial spacing (2.1–3.5 mm) results from the geometric arrangement required to maintain concentricity between layers and to distribute channels homogeneously across the wheel width.

Earlier investigations based on Taguchi analysis and CFD revealed a general trend that larger channel diameters promoted superior hydraulic behavior [43]. Since in that case the number of channels and outlet area were not constant, the present study was designed with a fixed outlet area to isolate the diameter effect and better evaluate its practical implications.

The three configurations developed are summarized in Table 1.

2.2. CFD methodology

The behavior of the fluid flow through the structured grinding wheels was analyzed using numerical simulations performed in ANSYS Fluent 2022. The three-dimensional model consists of an abrasive grinding wheel with internal channels, positioned 1 mm from the surface of the part, as shown in Fig. 2. The geometry presented in this figure corresponds to the GW_69_1.0 configuration, used as a representative example. The coolant fluid (water) is injected axially through the shaft, distributing itself through the channels until reaching the contact zone. To represent the external environment and capture the dispersion of fluid after exiting the wheel, the computational domain was enclosed by

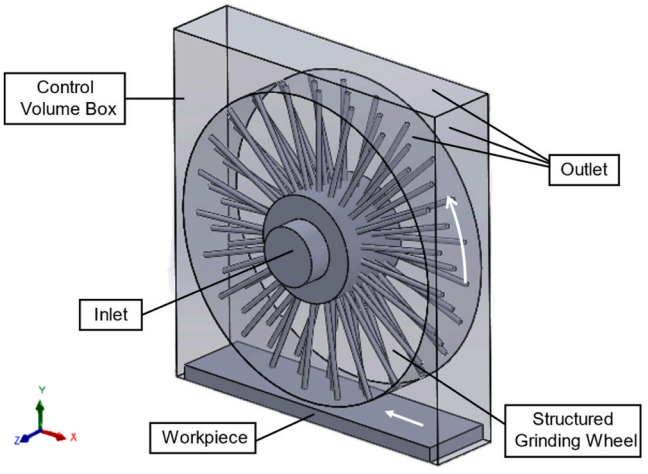

Fig. 2. 3D model of the computational domain showing the structured grinding wheel (GW_69_1.0), the workpiece, the control volume box, and the inlet/outlet regions. The rotation direction of the wheel is also indicated.

Table 1
Geometric specifications of the structured grinding wheels evaluated in this study.

Grinding Wheel	Channel Diameter (mm)	Total Number of Channels	Channels per Layer	Number of Layers	Interlayer Distance (mm)	Total Outlet Area (mm^2)
GW_190_0.6	0.6	190	38	5	1.5	53.7
GW_69_1.0	1.0	69	23	3	2.5	54.2
GW_30_1.5	1.5	30	10	3	2	53.0

a control volume box with dimensions of 66 × 68 × 15 mm^3 (X × Y × Z). The wheel geometry was modeled based on the actual dimensions of the sintered tools described previously.

The mesh was primarily composed of hexahedral elements, with local refinement in the internal channels, the central shaft, and the outlet region to ensure accurate resolution of the flow gradients. To capture near-wall effects, six inflation layers were applied along the internal channel walls, with a first-layer thickness of 0.1 mm and a growth rate of 1.2. The external control volume (air domain) was progressively coarsened away from the wheel surface to reduce computational cost while maintaining sufficient accuracy in the jet dispersion zone. The final grid contained approximately 3.3 million elements, a value determined through a mesh independence study, in which variations in the average outlet velocity and jet dispersion pattern were below 2 % when compared to a finer mesh (≈ 4.2 million cells).

The grinding wheel was modeled as a non-porous solid, and the two-phase flow (water–air) was solved under steady-state conditions. The rotation of the wheel at 5000 rpm, matching the experimental setup, was simulated using the Multiple Reference Frame (MRF) approach [53]. The implicit formulation was selected to enhance numerical stability and reduce processing time [54–56], while the dispersed phase option was activated to represent water droplets transported within the continuous air phase [57]. The surface tension between air and water was set to 0.0728 N/m [51,58] and gravity was applied toward the workpiece to reproduce the real orientation of the grinding system.

Based on the estimated Reynolds numbers (Re < 2000), the flow inside the channels is laminar for all three geometries. However, this model was designed to analyze the dispersion of coolant in the external environment, including the mixing of water jets with air and their impact on the workpiece surface. Once the jets emerge from the channels, they are subjected to strong shear instabilities (e.g., Kelvin–Helmholtz mechanisms), which can rapidly promote transition and turbulence [50,59,60]. Widely employed in industrial applications involving turbulent flows, such as flow around solid surfaces and fluid jets, the $k-\varepsilon$ (2 eqn) realizable model was the turbulence model chosen [47,61]. The realizable version was chosen for its robustness in improving the accuracy of highly distorted flows, such as those occurring in the interaction between the coolant and the workpiece [16,57].

Boundary conditions were defined as follows: a uniform mass-flow inlet of 0.0067 kg/s (400 mL/min) at the shaft entrance, corresponding to the experimental flow rate; an ambient-pressure outlet applied to all external faces of the control volume; and smooth, no-slip wall conditions on all solid surfaces (wheel, shaft, and workpiece). These conditions ensured consistency between the numerical and experimental configurations. The main outputs were the velocity fields (contours and vectors) near the wheel surface, used to evaluate the coolant distribution and its intensity toward the contact zone.

A separate set of simplified simulations was carried out to evaluate the outlet velocity profiles at the channel exits. In this case, only water was considered (single–phase flow), and the external control volume was removed, restricting the domain to the wheel and its internal channels. This modification avoided the numerical limitation of the full model, where the outlet coincides with a rotating wall. In the simplified configuration, the velocity field was computed in the relative reference frame, so that the no-slip condition at the channel walls was correctly imposed and the jet profiles could be extracted without the artificial offset introduced by the absolute formulation. The resulting outlet distributions reflected the effective jet momentum generated by the internal flow, enabling quantitative comparison among the different geometries. The mesh contained approximately 1.2 million elements, generated with the same refinement strategy and quality criteria adopted in the full simulations. All other boundary conditions and convergence parameters were also kept consistent.

Velocity profiles were extracted through cross-sectional planes orthogonal to the channel exit. To provide a comparative indicator of hydraulic utilization, the fraction of the channel area with very low velocities was quantified. A threshold of 0.1 m/s was adopted, corresponding to the lower end of the velocity scale observed in the simulations (0–1 m/s). In the velocity contour maps, this range appears as the blue regions, which were segmented using ImageJ software. These regions were considered hydraulically inefficient, as their contribution to jet momentum and coolant transport toward the contact zone is expected to be negligible. The fraction of this low-velocity area relative to the total channel cross-section was then used as a comparative metric among the different geometries.

The simulated outlet velocity were experimentally validated by tracking individual coolant particles using the TrackMate plugin in *Fiji*, following the methodology described in Costa et al. (2025) [62].

2.3. Experimental setup

The grinding tests were performed in up-grinding mode, using a surface grinding machine. The grinding wheel was operated at 5000 rpm, which corresponds to a peripheral speed of 16.23 m/s, while the feed table was maintained at 100 mm/min. Six cutting depths were evaluated: 10, 20, 50, 80, 100 and 120 μm, applied to each of the three structured grinding wheels. Before each test, the grinding wheel was dressed using a multi-point diamond dresser under identical conditions ($\boldsymbol{v_s} = 1000$ rpm, $\boldsymbol{v_w} = 100$ mm/min, $\boldsymbol{a_p} = 30$ μm), in order to restore the cutting surface and minimize the influence of wheel topography on the measured forces and temperatures.

Lubrication was applied internally, with distilled water injected directly into the machine spindle and flowing through the radial channels toward the contact zone. Distilled water was selected as the cutting fluid due to its well-known thermal properties, stability, and reproducibility in controlled experiments. While this does not replicate industrial practice, the purpose of this study was to isolate the effect of channel geometry on cooling and lubrication. Using water avoids the influence of additives and contaminants present in industrial coolants, ensuring that performance differences could be attributed solely to the internal fluid delivery configuration.

The inflow rate was fixed at 400 mL/min, controlled by a peristaltic pump connected to the spindle inlet, ensuring a constant volumetric supply independent of wheel rotation. This value was selected based on preliminary experiments and CFD analyses [43,62,63]. Although centrifugal effects redistribute the fluid inside the wheel, the total mass flow delivered to the outlet channels remains fixed by the pump.

The workpieces were made of AISI 1045 steel, with dimensions of 80 × 15 × 10 mm. All samples were previously ground to ensure parallelism and uniform surface finish. Fig. 3 presents an overview of the experimental system, highlighting the structured grinding wheel, the part, the temperature sensor and the positioning of the load cell. Inside the grinding wheel, the cutting fluid is injected through an axial system, ensuring a controlled pressurization of the central chamber. This internal pressure is sufficient to force the fluid to flow through the radial channels of the grinding wheel, promoting its efficient expulsion to the contact zone during the grinding process. The internal structure of the wheel and channel layout were previously described in Fig. 1.

The instrumentation included a TAS3F load cell, installed under the grinding machine table, for continuous measurement of normal (F_n) and tangential (F_t) forces. The force ratio was adopted as an indicator of the tribological behavior of the system and calculated as shown in Eq. (1):

$$Force\ ratio = \frac{F_t}{F_n} \tag{1}$$

The specific grinding energy (Ec) was determined to evaluate the energy efficiency of the material removal process for each wheel configuration, according to Eq. (2) [64]:

$$Ec = \frac{F_t . v_s}{Q_w} \tag{2}$$

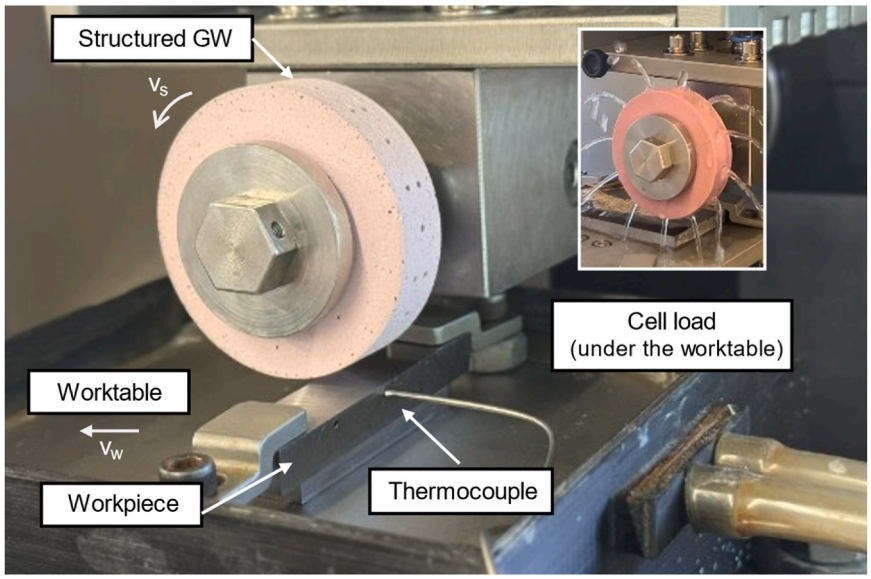

Fig. 3. Experimental setup showing the structured grinding wheel, workpiece, feed and rotation directions, and sensor locations.

where F_t is the tangential grinding force (N), v_s is the cutting speed (m/s), and Q_w is the material removal rate (mm^3/s).

Temperature was recorded at 5 Hz using a K-type thermocouple positioned 1 mm from the surface and analyzed based on the thermal variation (ΔT), defined as the difference between the initial temperature (before the grinding wheel contacted the workpiece) and the maximum value recorded during the test.

To ensure reproducibility, three repetitions were performed for each experimental condition, and the results presented in the figures correspond to the mean values ± standard deviation. All tests were conducted under controlled room

temperature, with consistent dressing parameters and data-acquisition settings to minimize random variability. The main operational and instrumentation parameters are organized in Table 2. The operating parameters adopted in this study were established based on preliminary grinding trials and previous investigations using the same test rig and workpiece material [43,62,63]. These conditions ensured process stability and measurable thermal and mechanical responses, while remaining within the typical industrial range for surface grinding with vitrified alumina wheels.

3. Results and analysis

The performance of the structured grinding wheels was analyzed through CFD simulations and experimental tests, focusing on how variations in channels geometry, specifically channel diameter, affect the system's behavior. Although all configurations were designed with similar outlet areas, the internal fluid dynamics and grinding responses differed significantly. The following sections present and discuss the numerical and experimental results, highlighting the influence of channel arrangement on fluid distribution, grinding forces, temperature, and derived parameters such as force ratio and specific grinding energy.

Table 2
Operational parameters and instrumentation used in the grinding tests.

Parameter	Value
Wheels tested	GW_190_0.6; GW_69_1.0; GW_30_1.5
Wheel dimensions	62 × 15 mm
Workpiece	AISI 1045 (80 ×15 ×10 mm); 198 HV
Depths of cut (a_p)	10, 20, 50, 80, 100, 120 μm
Wheel peripheral speed (v_s)	16.23 m/s (5000 rpm)
Table feed rate (v_w)	100 mm/min
Coolant	Distilled water
Flow rate	400 mL/min
Lubrication System	Internal (via radial channels)
Dressing conditions	$v_s = 1000rpm$; $v_w = 100mm/min$; $a_p = 30\mu m$

3.1. Numerical analysis

The numerical results were divided into two complementary analyses: first, the flow distribution and velocity vectors on the wheel surface were examined using the full CFD model; then, simplified simulations were performed to extract the outlet velocity profiles and identify regions of low hydraulic utilization.

Fig. 4 shows the velocity vectors on the external surface of the grinding wheel for the three geometries evaluated, covering both the outlet of the channels and the contact zone with the workpiece. GW_190_0.6 promotes a high density of vectors distributed over the surface, favoring broad coverage, but with low flow intensity, a behavior that reflects the limited capacity of narrow channels to sustain strong jet momentum. The GW_30_1.5 wheel concentrates more intense jets in specific regions, with large spacing between them, which can lead to the formation of zones with insufficient fluid supply. The GW_69_1.0 configuration exhibits an intermediate pattern, combining reasonably strong jets with more uniform coverage across the tool surface.

To further investigate the local fluid performance at each channel outlet, velocity profiles were extracted from a simplified CFD setup. Table 3 presents the average outlet velocities and the corresponding area and percentage of regions with velocities below 0.1 m/s, indicative of regions with low hydraulic utilization. Fig. 5 shows the velocity profiles on the outlet surface, highlighting areas of low (blue) and high (red) flow.

The GW_190_0.6 setup had the lowest average speed (0.45 m/s) and the biggest percentage of region with slow flow (19 %). This behavior results from the high number of narrow channels, which increase pressure losses due to internal wall friction. As the channel diameter increases, these losses are reduced. This is shown by the higher speeds shown in GW_69_1.0 (0.75 m/s) and GW_30_1.5 (0.80 m/s), which are also shown by the lower area fractions with $V < 0.1$ m/s (14 % and 7 %, respectively). However, the additional gain between the Ø 1.0 mm and Ø 1.5 mm configurations is modest, which suggests that the hydraulic performance is reaching a limit.

To provide a geometric interpretation of these hydraulic differences, a Geometric Flow Index (GFI) was defined as the ratio between the total channel volume and the corresponding internal wall area. This index

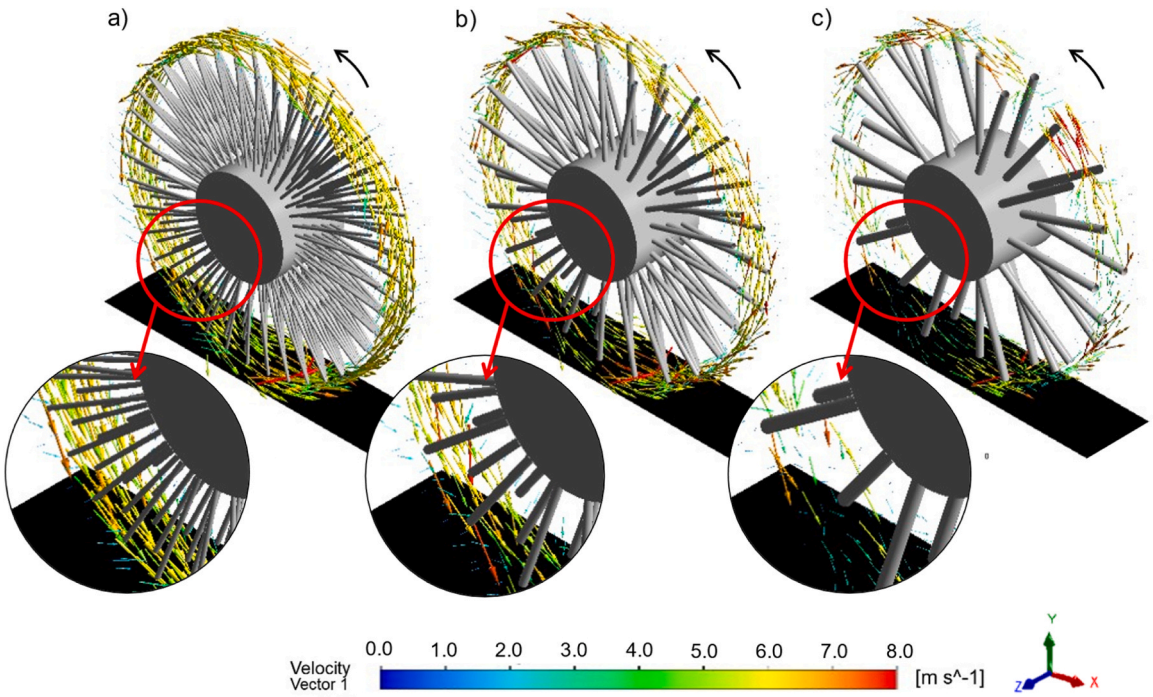

Fig. 4. Velocity vectors obtained from CFD simulations on the external surface of the grinding wheels and in the contact zone with the workpiece: (a) GW_190_0.6, (b) GW_69_1.0, and (c) GW_30_1.5.

Table 3
Average outlet velocity and fraction of low-velocity regions (V < 0.1 m/s) for the three structured wheel configurations.

Grinding Wheel	Average velocity (m/s)	Total outlet area (mm^2)	Area with V < 0.1 m/s (mm^2)	Area with V < 0.1 m/s (%)
GW_190_0.6	0.45	53.7	10.2	19
GW_69_1.0	0.75	54.2	7.5	14
GW_30_1.5	0.80	53.0	3.8	7

reflects the relative balance between flow capacity and internal resistance imposed by channel walls. As shown in Fig. 6, the percentage of low-velocity regions (<0.1 m/s) decreases linearly with increasing GFI, indicating a direct relationship between wall friction and energy losses. In contrast, the average outlet velocity increases up to a GFI of approximately 0.25, beyond which it stabilizes. This suggests that while increased GFI reduces frictional losses and improves flow efficiency, its effect on outlet speed becomes marginal beyond this threshold.

The distribution observed in GW_69_1.0 appears to balance surface coverage and velocity magnitude, with moderately strong jets more evenly distributed across the wheel surface. This configuration suggests a compromise between the broad, low-momentum flow of GW_190_0.6 and the concentrated high-velocity jets of GW_30_1.5. Further analysis in the following sections explores how this intermediate behavior affects fluid effectiveness in the cutting zone.

3.2. Grinding tests

Experimental tests were conducted on the structured wheels to validate numerical predictions and assess the effects of channel geometry on grinding forces, friction coefficient, specific grinding energy, and thermal behavior.

Figs. 7a and 7b, together with Table 4, show the average values of the tangential (F_t) and normal (F_n) forces as a function of the depth of cut. The GW_190_0.6 and GW_30_1.5 configurations showed similar forces

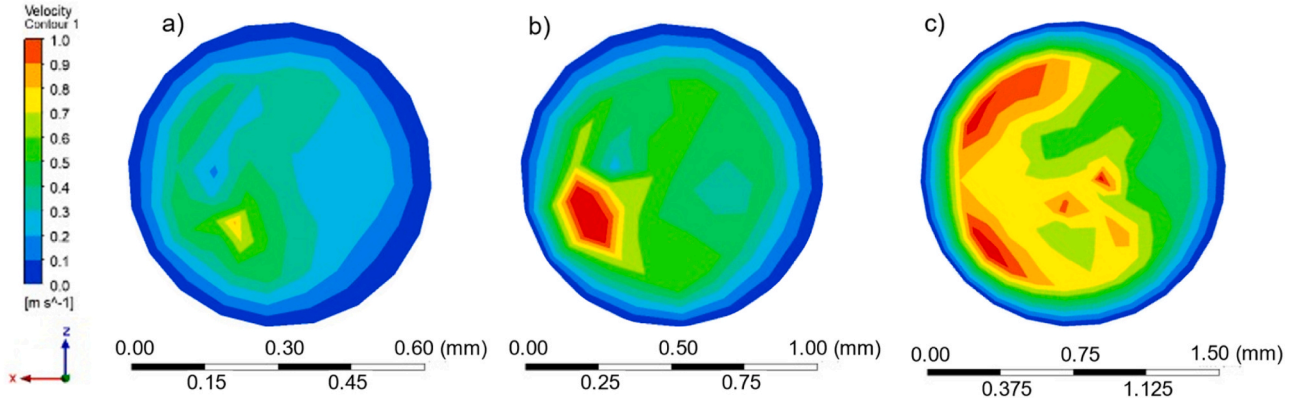

Fig. 5. Velocity contour maps obtained from CFD simulations at the outlet surface of the structured grinding wheels: (a) GW_190_0.6, (b) GW_69_1.0, and (c) GW_30_1.5. The color scale represents local fluid velocity, highlighting low-velocity regions (blue) and high-velocity jets (red). The horizontal scale below each map indicates the physical size of the corresponding channel outlet (mm).

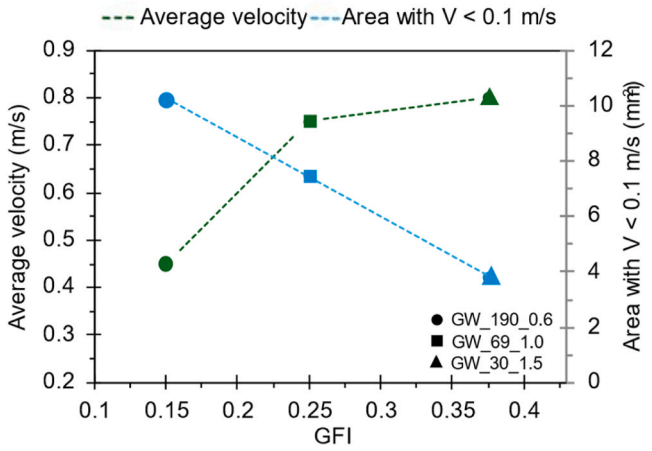

Fig. 6. Relationship between the Geometric Flow Index (GFI), average outlet velocity, and low-velocity area (V < 0.1 m/s) obtained from CFD simulations for the three grinding wheel configurations. The GFI represents the ratio between total channel volume and internal wall area, indicating the balance between flow capacity and hydraulic resistance.

throughout the tested range. The grinding wheel with Ø 1.0 mm 1.0 mm channels (GW_69_1.0) presented the lowest values in all conditions, with emphasis on the reductions of 38 % in F_t (at 10 μm) and 26 % (at 50 μm), compared to the Ø 1.5 mm configuration, evidencing its greater efficiency in reducing the cutting effort. These trends were consistently observed across the three repetitions, with a maximum standard deviation of 0.42 N in the force measurements.

Fig. 8 shows the force ratio (F_t/F_n) as a function of the cutting depth for the three configurations evaluated. This parameter expresses the relationship between tangential and normal grinding forces and is commonly used to assess the efficiency and nature of the grain–workpiece interaction. It can be observed that all geometries exhibit lower force ratio values at the initial depths (10–20 μm), followed by a progressive increase with increasing penetration. This trend suggests a transition in the tribomechanical regime: at shallow depths, the lower load per grain and limited material removal promote conditions closer to sliding contact. As the depth increases, grain engagement becomes more significant, abrasive interactions intensify, and the process evolves toward a more stable cutting regime. The GW_69_1.0 grinding wheel exhibited the lowest force ratio values across the entire range, indicating a more consistent interaction with the workpiece and improved overall performance. In contrast, the GW_190_0.6 and GW_30_1.5 configurations showed a more pronounced increase in force ratio, suggesting less stability in grain–workpiece interactions and a possible deficit in fluid delivery under intermediate cutting conditions.

Fig. 9 shows the variation of specific cutting energy as a function of cutting depth. The GW_190_0.6 and GW_30_1.5 geometries presented the highest specific energy values at the shallowest depths (10–20 μm), with a tendency to progressively reduce from 50 μm onwards. This behavior indicates low energy efficiency in the initial passes, possibly due to the predominance of surface plastic deformation mechanisms and friction without effective cutting. As the depth increases, grain penetration improves and the shear removal regime stabilizes, reducing energy consumption per volume removed. In contrast, the GW_69_1.0 grinding wheel maintained low and more constant specific energy values throughout the analyzed range, suggesting a more favorable energetic response at the tested range of cutting. This difference highlights the influence of the channel's configuration on the lubrication dynamics and the cutting regime established in each case.

The combined analysis of Figs. 8 and 9 reveals that a low force ratio value does not necessarily imply an energy-efficient process. Configurations GW_190_0.6 and GW_30_1.5 presented low F_t/F_n values at shallower depths (10–20 μm), but associated with high specific energy values, which indicates low material removal efficiency under these conditions. This behavior can be explained by the predominance of surface plastic deformation, associated with low grain penetration and friction without effective cutting, a phenomenon described as plowing [5,65–67]. In these cases, although the tangential force is not significant, the normal force is relatively high due to the surface stiffness and the contact distributed by many grains that only slide over the part. As a result, the force ratio is numerically low, but the energy consumed per removed volume is high, reflecting an inefficient tribological regime.

On the other hand, the GW_69_1.0 configuration demonstrated a different behavior: it maintained a low and stable force ratio even at shallow depths, with equally low and constant specific energy values. This indicates that, in this case, there is in fact an effective shear removal of material, with a lower contribution of plastic deformation. This performance suggests that the Ø 1.0 mm channels provided more effective lubrication, allowing adequate penetration of the grains from the first passes, without depending on the stabilization of the cutting regime at greater depths.

Therefore, the comparison between the three geometries reinforces that a low force ratio can only be interpreted as an indicator of efficiency when correlated with other parameters, such as specific energy, cutting forces, and temperature. In the case of the GW_190_0.6 and GW_30_1.5 grinding wheels, the low force ratio values at shallow depths do not reflect a favorable cutting condition, as they coincide with high energy consumption and suggest the presence of friction-dominated contact and surface plastic deformation, intensified by ineffective lubrication, either due to low flow velocity (Ø 0.6 mm) or limited fluid coverage (Ø 1.5 mm). Only the Ø 1.0 mm grinding wheel configuration exhibited a coherent and efficient interaction between frictional behavior, energy consumption, and grain penetration.

Fig. 10, together with Table 5, presents the maximum temperature

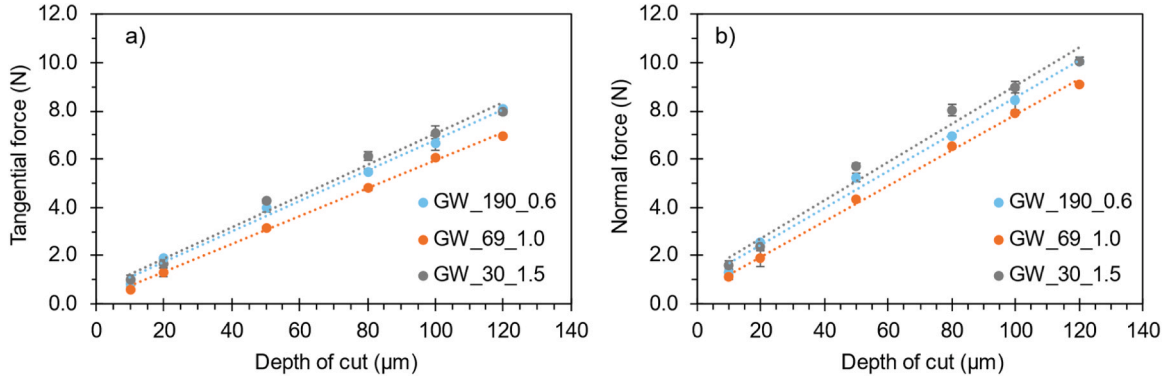

Fig. 7. Tangential (a) and normal (b) grinding forces as a function of cutting depth for the structured vitrified wheels with internal channels (GW_190_0.6, GW_69_1.0, and GW_30_1.5). Each point represents the average of three repetitions, with error bars indicating standard deviation.

Table 4
Average tangential and normal forces and their respective standard deviations, obtained from three repeated grinding tests for each wheel geometry and depth of cut.

Depht of cut (μm)	Tangential Force			NormalForce		
	GW_190_0.6 (N)	GW_69_1.0 (N)	GW_30_1.5 (N)	GW_190_0.6 (N)	GW_69_1.0 (N)	GW_30_1.5 (N)
10	0.82 ± 0.12	0.63 ± 0.04	1.02 ± 0.17	1.32 ± 0.14	1.11 ± 0.09	1.62 ± 0.20
20	1.91 ± 0.03	1.32 ± 0.21	1.67 ± 0.15	2.57 ± 0.03	1.91 ± 0.36	2.36 ± 0.18
50	3.99 ± 0.16	3.15 ± 0.06	4.26 ± 0.06	5.24 ± 0.20	4.32 ± 0.05	5.74 ± 0.10
80	5.51 ± 0.08	4.81 ± 0.09	6.14 ± 0.17	6.98 ± 0.05	6.52 ± 0.01	8.03 ± 0.24
100	6.66 ± 0.30	6.08 ± 0.06	7.11 ± 0.27	8.43 ± 0.42	7.94 ± 0.03	9.00 ± 0.23
120	8.12 ± 0.05	6.97 ± 0.06	8.00 ± 0.14	10.06 ± 0.00	9.13 ± 0.01	10.09 ± 0.16

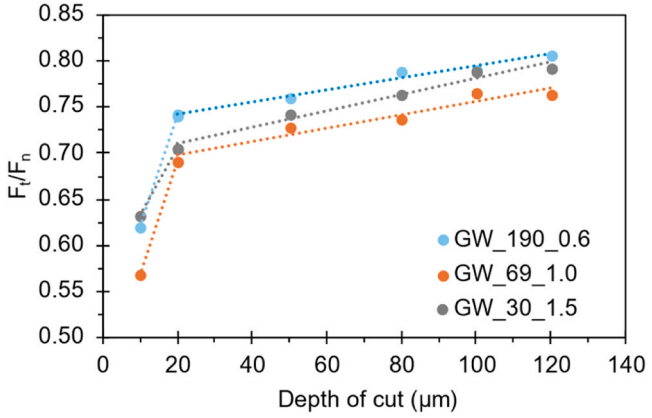

Fig. 8. Variation of the force ratio (Ft/Fn) with cutting depth for the structured vitrified grinding wheels (GW_190_0.6, GW_69_1.0, and GW_30_1.5). The plotted values represent the mean of three repetitions for each condition.

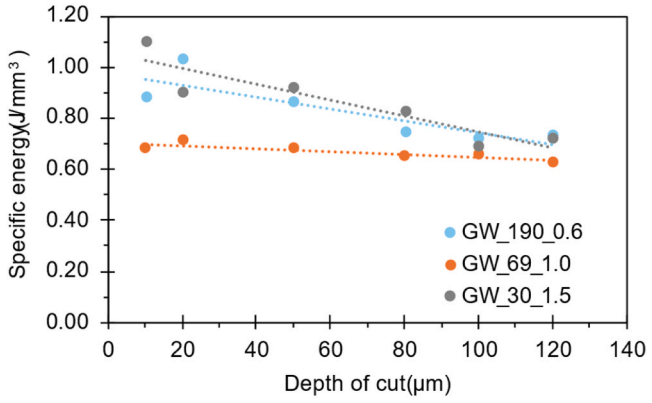

Fig. 9. Specific grinding energy as a function of cutting depth for the structured vitrified wheels with different internal channel diameters. The specific energy was calculated from the measured tangential force and the material removal rate.

variation (ΔT) in the workpiece as a function of cutting depth. The GW_190_0.6 configuration recorded the highest ΔT values under all conditions, while the GW_69_1.0 wheel showed the lowest average temperatures, with reductions of 40.9 % and 30.1 % at 50 μm and 100 μm, respectively, when compared to GW_190_0.6. This behavior reinforces the importance of fluid distribution and surface coverage in thermal dissipation during grinding. As demonstrated by Liu et al. [2], increasing the normal grinding force intensifies the elastic deformation of the grinding wheel, which enlarges the contact arc and increases the number of active cutting grains. Consequently, the heat-affected zone expands, and surface temperature rises progressively. Therefore, the lower ΔT observed in GW_69_1.0 may be attributed not only to improved fluid penetration but also to a more favorable balance

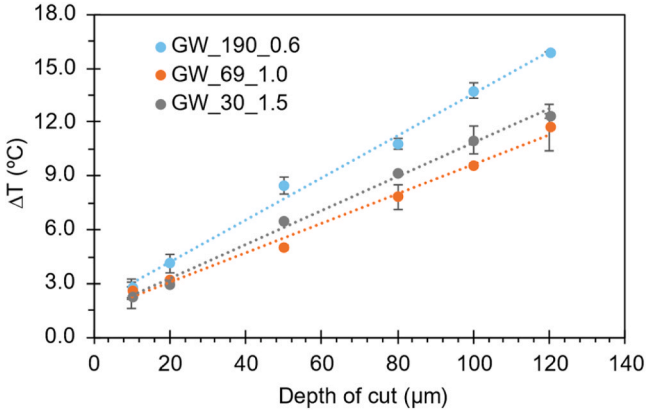

Fig. 10. Temperature variation (ΔT) in the workpiece as a function of cutting depth for the structured vitrified wheels with internal channels. The temperature was measured using a K-type thermocouple embedded 1.0 mm below the workpiece surface. Reported values correspond to the average of three repetitions, with error bars indicating standard deviation.

Table 5
Temperature variation (ΔT) and standard deviation for the three grinding wheel geometries at each depth of cut.

Depht of cut (μm)	GW_190_0.6 (°C)	GW_69_1.0 (°C)	GW_30_1.5 (°C)
10	2.75 ± 0.50	2.58 ± 0.46	2.24 ± 0.59
20	4.12 ± 0.54	3.19 ± 0.06	2.98 ± 0.06
50	8.46 ± 0.48	5.00 ± 0.13	6.47 ± 0.07
80	10.80 ± 0.30	7.83 ± 0.68	9.20 ± 0.05
100	13.75 ± 0.40	9.61 ± 0.15	11.00 ± 0.76
120	15.90 ± 0.15	11.70 ± 1.27	12.38 ± 0.13

between jet velocity and surface coverage, which helps limit thermal accumulation even as the contact area increases with cutting depth. These trends were consistently reproduced across the repetitions, with maximum standard deviations of 0.69 °C for low and moderate depths (≤80 μm), and values ranging between 0.15 and 1.27 °C at the higher depths of cut (100–120 μm).

Overall, the experimental results demonstrated distinct performance patterns among the tested grinding wheel configurations. While each design presented advantages under specific conditions, the GW_69_1.0 configuration consistently delivered lower forces, friction, and temperature variation across all cutting depths. These findings suggest that geometric parameters, particularly channel diameter and distribution, play a critical role in defining the efficiency of internal lubrication.

An additional aspect to be considered is the potential effect of internal channels on wheel wear. On the one hand, the enhanced coolant transport and improved removal of grinding debris would be expected to reduce wheel loading and thermal damage, thereby mitigating wear progression, as already demonstrated in the literature [41,68]. On the other hand, the presence of channels decreases the effective cutting area and introduces edges that may act as local stress concentrators, which could accelerate wear at specific regions. Nevertheless, it should be

noted that the total active surface of the wheel (~2922 mm²) is only slightly reduced by the channel outlets (~54 mm²), corresponding to less than 2 % of the total.

A complementary indication of this trend can be drawn from a previous study in which vitrified alumina wheels incorporating superficial spiral and hexagonal channels were evaluated under pin-on-disk conditions [69]. In that work, the presence of channels led to a reduction in wheel wear of approximately 35 % (hexagonal) and 42 % (spiral), together with an increase in grinding ratio of up to 153 % when compared with a conventional wheel. Although obtained with surface-textured rather than internally channel-integrated wheels, these results reinforce the expectation that improved coolant access and debris evacuation tend to mitigate wear progression.

3.3. Correlation between CFD and experimental results

This section establishes the correlation between the CFD predictions and the experimental results, linking the simulated outlet flow characteristics to the measured mechanical and thermal responses during grinding. The comparative analysis revealed clear correspondences between the fluid behavior at the channel outlets and the overall grinding performance.

The GW_190_0.6 configuration exhibited lower tangential and normal forces than GW_30_1.5, despite its poorer performance in temperature control and force ratio. This behavior may be related to the more homogeneous surface coverage provided by the higher number of channels, even with lower outlet velocity. Such distribution tends to reduce the local heat produced by mechanical interaction peaks and micro-impacts between the tool and the workpiece. In contrast, the concentrated and high-velocity jets in the GW_30_1.5 configuration favor localized heat removal but result in less uniform lubrication, which can generate localized mechanical stresses at the abrasive grain–workpiece interface.

Regarding thermal behavior, the GW_30_1.5 configuration performed better at lower cutting depths (10–20 μm), likely due to the focused action of the more intense jets, promoting effective localized cooling. However, above 50 μm, its performance became inferior to that of GW_69_1.0. This change can be explained by the more limited surface coverage of the widely spaced channels, whose effectiveness decreases as the contact area increases, making it difficult to maintain adequate cooling under more demanding conditions.

Fig. 11 shows the relationship between the outlet area fraction with velocity below 0.1 m/s and the experimental results for tangential force (a) and maximum temperature variation (b). As only three wheel geometries were evaluated, this comparison is intended as a qualitative assessment of the tendencies between the CFD parameter and the experimental behavior. Tangential force remains nearly unchanged as this variable increases, indicating that mechanical behavior is not strongly influenced by the low-velocity outlet area. In contrast, temperature exhibits an upward tendency, suggesting that thermal performance is more sensitive to the coolant velocity distribution at the outlet. This distinction supports the interpretation that fluid delivery with sufficient velocity is essential for effective heat removal at the contact zone, whereas force levels depend more closely on jet orientation, coverage and the resulting lubrication conditions.

At higher cutting depths, however, the behavior does not follow the same clear tendency observed at 10 μm. Grinding is a thermally complex process, and several mechanisms contribute simultaneously to heat generation and removal. At low depths, such as 10 μm, the measured temperature in the workpiece follows closely the fraction of low-velocity outlet area, with smaller low-velocity regions resulting in lower ΔT. At 50 and 120 μm, the tendency becomes less clear, indicating that coolant velocity alone is not sufficient to ensure effective heat dissipation under more demanding conditions. Increased heat generation, a larger contact area and a higher chip volume all begin to play a more significant role, making the thermal response more complex as cutting depth increases. To better understand these interactions, a dedicated experimental program will be required, including temperature-profile measurements at multiple locations rather than relying solely on the maximum temperature value, as performed in the present study.

Fig. 12 illustrates the correspondence between the simulated velocity distribution at the channel outlets and the flow patterns observed on the grinding wheels experimentally. To enhance visual identification of fluid dispersion, a coulorant was added to the distilled water used in the experimental setup. It should be noted that, due to the use of the colorant, the outlet regions of the jets, corresponding to the more covered areas, appear highlighted in blue on the wheel surface. The channel geometry influences not only the jet intensity but also the uniformity and extent of fluid distribution over the wheel surface. The GW_190_0.6 configuration shows multiple visible outlet points, with weaker but well-distributed jets, matching the continuous and homogeneous pattern predicted in the simulation. The GW_69_1.0 configuration combines moderate jet intensity with a relatively uniform distribution, which aligns with its balanced performance observed in the experiments. In contrast, the GW_30_1.5 configuration concentrates the fluid output in fewer points, with intense jets that are less visible on the wheel surface, reflecting the lower surface coverage predicted in the simulation, especially in the regions between channels.

This direct comparison between simulation and experimental observation reinforces the reliability of the CFD modeling approach and highlights its potential as a design support tool for structured grinding wheels with improved hydraulic and thermal performance.

The results obtained with optimized internal channels geometries have potential direct application in industrial systems seeking greater sustainability and efficiency in the grinding process. The possibility of reducing cutting efforts and temperature without changes on the fluid consumption allows for greater tool durability and lower environmental impact. In addition, the adopted methodology, which combines CFD

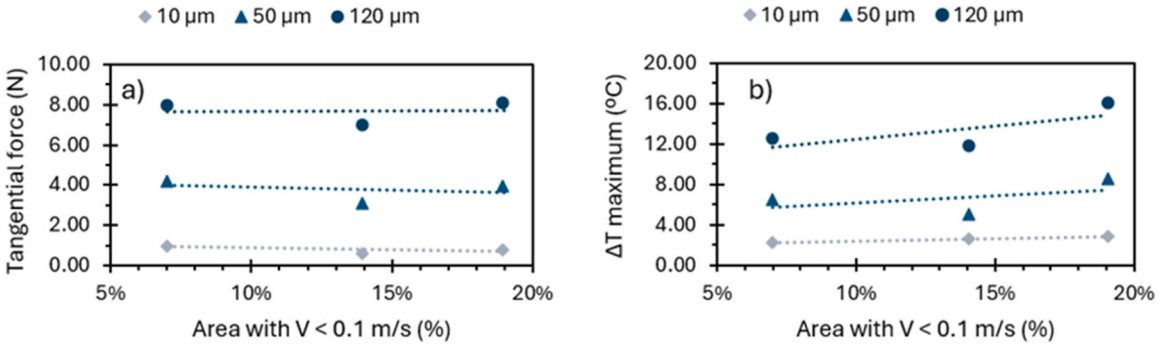

Fig. 11. Correlation between the outlet area fraction with velocity below 0.1 m/s (from CFD simulations) and experimental results: (a) tangential grinding force and (b) maximum temperature variation for three cutting depths (10, 50, and 120 μm).

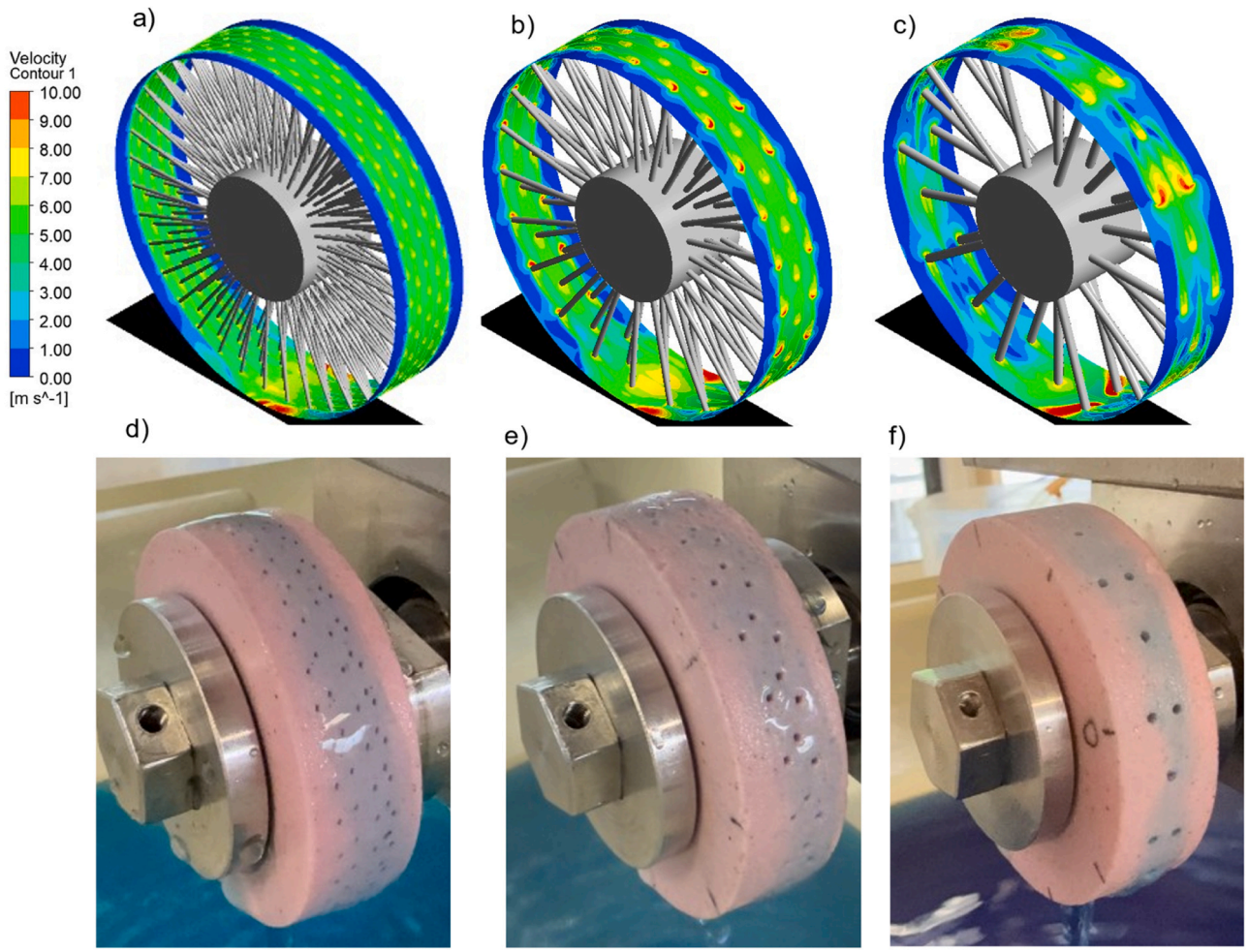

Fig. 12. Velocity distribution at the channel outlets obtained from CFD simulations (a–c) and corresponding fluid ejection observed on the grinding wheel surface during operation (d–f): (a, d) GW_190_0.6, (b, e) GW_69_1.0, and (c, f) GW_30_1.5. The images illustrate the agreement between simulated and experimental flow patterns, where blue regions indicate areas of greater fluid coverage on the wheel surface.

simulations with tests on real vitrified grinding wheels, can be extended to the analysis of other metal alloys (such as stainless steel or superalloys) or to different channel configurations (e.g., inclined, helical, combined).

4. Conclusion

This study investigated the influence of channel diameter on the hydraulic and tribological performance of internally cooled vitrified grinding wheels, maintaining a constant total outlet area. The main conclusions can be summarized as follows:

1. CFD simulations demonstrated that channel geometry governs the trade-off between outlet velocity and surface coverage. Narrow channels (Ø 0.6 mm) produced homogeneous but low-intensity flow due to higher hydraulic resistance, while wide channels (Ø 1.5 mm) generated stronger jets but less uniform fluid distribution.
2. Experimental results confirmed these tendencies quantitatively: the intermediate design (Ø 1.0 mm) achieved up to 38 % lower tangential force and 41 % lower temperature rise compared with the narrow-channel wheel, while maintaining low specific grinding energy across all cutting depths.
3. Quantitative correlation between CFD and experiments showed that the fraction of low-velocity regions ($V < 0.1$ m/s) at the channel outlets is directly linked to the measured thermal response: higher low-velocity fractions corresponded to greater temperature rise, confirming the sensitivity of cooling performance to outlet flow uniformity.

Overall, these findings show that channel diameter and quantity must be jointly optimized to ensure efficient internal cooling. Tailoring channel geometry can significantly reduce mechanical loads, stabilize grinding performance, and lower coolant consumption, contributing to more sustainable grinding processes.

CRediT authorship contribution statement

Mário Pereira: Writing – review & editing, Supervision, Resources, Investigation, Data curation. **Delfim Soares:** Writing – review & editing, Validation, Supervision, Resources, Methodology, Funding acquisition, Formal analysis, Conceptualization. **Sharlane Costa:** Writing – review & editing, Writing – original draft, Software, Methodology, Investigation, Formal analysis, Conceptualization. **Amauri Hassui:** Writing – review & editing, Resources, Methodology. **Ribeiro J.E.:** Writing – review & editing, Supervision, Software, Investigation, Data curation, Conceptualization. **Paulina Capela:** Writing – review & editing. **Maria Sousa:** Writing – review & editing, Data curation.

Declaration of Competing Interest

The authors of this work declare that there is no conflict of interest.

Acknowledgements

This work was supported by FCT (Foundation for Science and Technology) national funds, under the national support to R&D units grant, through the reference project UIDB/04436. The authors are grateful to the Foundation for Science and Technology (FCT, Portugal) for financial support through national funds FCT/MCTES (PIDDAC) to CIMO (UIDB/00690/2020 and UIDP/00690/2020) and SusTEC (LA/P/0007/2020). This work is within the scope of Sharlane Costa Ph.D. degree, in progress, financially supported by the Portuguese Foundation for Science and Technology (FCT) through the Ph.D grant reference 2021.07352.BD (DOI:https://doi.org/10.54499/2021.07352.BD). Paulina Capela acknowledges the financial support from FCT through the doctoral grant 2024.01273.BDANA.

Data availability

No data was used for the research described in the article.

References

[1] P. Capela, S. Costa, M.S. Souza, S. Carvalho, M. Pereira, L. Carvalho, J.R. Gomes, D. Soares, Wear behavior of a new composite formulation, with TEOS addition, for abrasive vitrified grinding wheels, Wear 512–513 (2023) 204524, https://doi.org/10.1016/J.WEAR.2022.204524.

[2] S. Liu, Y. Tian, B. Liu, G. Zhang, J. Han, H. Yun, Modeling and simulation of temperature field in high-shear and low-pressure grinding with liquid-body-armor-like grinding wheel, J. Manuf. Process 124 (2024) 1080–1091, https://doi.org/10.1016/J.JMAPRO.2024.07.023.

[3] E. García, D. Méresse, I. Pombo, S. Harmand, J.A. Sánchez, Identification of heat partition in grinding related to process parameters, using the inverse heat flux conduction model, Appl. Therm. Eng. 66 (2014) 122–130, https://doi.org/10.1016/J.APPLTHERMALENG.2014.01.048.

[4] S. Huang, S. Liu, D. Wang, S. Wu, G. Wang, L. Wan, Q. An, L. Zhu, C. Li, Bio-inspired cutting tools: beneficial mechanisms, fabrication technology and coupling design, Sustain. Mater. Technol. 43 (2025) e01211, https://doi.org/10.1016/J.SUSMAT.2024.E01211.

[5] S. Malkin, C. Guo, 2007, Thermal Analysis of Grinding, Volume 56, Issue 2, Pages 760 - 782 56 (2007) 760–782. https://doi.org/10.1016/j.cirp.2007.10.005.

[6] K. Kishore, M.K. Sinha, A. Singh, Archana, M.K. Gupta, M.E. Korkmaz, A comprehensive review on the grinding process: advancements, applications and challenges, Proc. Inst. Mech. Eng. C. J. Mech. Eng. Sci. 236 (2022) 10923–10952, https://doi.org/10.1177/09544062221110782.

[7] K. Jayakumar, Effect of grinding parameters and coolants on grindability of Ti grade 9 alloy, Mater. Today Proc. (2024), https://doi.org/10.1016/j.matpr.2024.04.030.

[8] X. Fu, L. Lv, B. Chen, Z. Deng, M. Wu, Pre-control of grinding surface quality by data-driven: a review, Int. J. Adv. Manuf. Technol. 133 (2024) 3081–3104, https://doi.org/10.1007/s00170-024-13921-0.

[9] Y. Ran, J. Sun, R. Kang, Z. Dong, Y. Bao, Towards understanding the machining process in grinding of ceramic matrix composites: a review, Compos B Eng. 284 (2024) 111657, https://doi.org/10.1016/J.COMPOSITESB.2024.111657.

[10] J. Ge, Z. Deng, D. Cao, Z. Li, L. Lv, W. Liu, J. Nie, Study on modelling simulation and distribution characteristics of residual stress during robotic weld end grinding of high strength modulated steel, J. Manuf. Process 108 (2023) 98–113, https://doi.org/10.1016/J.JMAPRO.2023.10.052.

[11] N. Arunachalam, P. Suya Prem Anand, L. Vijayaraghavan, Investigation of tribological conditions on grinding of bioceramic material using diamond grinding wheel under different cooling and lubrication environment, J. Manuf. Process 71 (2021) 550–564, https://doi.org/10.1016/J.JMAPRO.2021.09.004.

[12] E. Ghadiri Zahrani, B. Azarhoushang, Laser conditioning of metal-bonded grinding wheel: effects of pulse durations and scanning directions on profile accuracy, Mater. Today Commun. 44 (2025) 112084, https://doi.org/10.1016/J.MTCOMM.2025.112084.

[13] S.M. Alimuzzaman, M.P. Jahan, C.S. Rakurty, N. Rangasamy, J. Ma, Cutting fluids in metal AM: a review of sustainability and efficiency, J. Manuf. Process 106 (2023) 51–87, https://doi.org/10.1016/J.JMAPRO.2023.09.075.

[14] Y. Lu, H. Huang, X. Rao, R. Mo, Y. Cai, Experimental study on dry electrical discharge truing of metal-bonded diamond wheel, Mater. Today Commun. 39 (2024) 109242, https://doi.org/10.1016/J.MTCOMM.2024.109242.

[15] C.Y. Wang, L. Zhang, C.F. Yang, Analysis and simulation of air flow field surrounding grinding wheel, Adv. Mat. Res 1027 (2014) 12–15, https://doi.org/10.4028/WWW.SCIENTIFIC.NET/AMR.1027.12.

[16] S. Majumdar, S. Mandal, I. Biswas, D. Roy, S. Chakraborty, Modelling of air boundary layer around the grinding wheel, Int. J. Model. Simul. 40 (2020) 104–113, https://doi.org/10.1080/02286203.2018.1562013.

[17] Y. Zhang, L. Li, X. Cui, Q. An, P. Xu, W. Wang, D. Jia, M. Liu, Y.S. Dambatta, C. LI, Lubricant activity enhanced technologies for sustainable machining: mechanisms and processability, Chin. J. Aeronaut. 38 (2025) 103203, https://doi.org/10.1016/j.cja.2024.08.034.

[18] X. Luo, S. Wu, D. Wang, Y. Yun, Q. An, C. Li, Sustainable development of cutting fluids: the comprehensive review of vegetable oil, J. Clean. Prod. 473 (2024) 143544, https://doi.org/10.1016/J.JCLEPRO.2024.143544.

[19] A. Elsheikh, A.B.M. Ali, A. Saba, H. Faqeha, A.A. Alsaati, A.M. Maghfuri, W. Abd-Elaziem, A.A. El Ashmawy, N. Ma, A review on sustainable machining: technological advancements, health and safety considerations, and related environmental impacts, Results Eng. 24 (2024) 103042, https://doi.org/10.1016/J.RINENG.2024.103042.

[20] A.K. Singh, A. Kumar, V. Sharma, P. Kala, Sustainable techniques in grinding: state of the art review, J. Clean. Prod. 269 (2020) 121876, https://doi.org/10.1016/J.JCLEPRO.2020.121876.

[21] K.C. Wickramasinghe, H. Sasahara, E.A. Rahim, G.I.P. Perera, Green metalworking fluids for sustainable machining applications: a review, J. Clean. Prod. 257 (2020) 120552, https://doi.org/10.1016/J.JCLEPRO.2020.120552.

[22] J.E. Manikanta, N. Ambhore, C. Nikhare, Application of sustainable techniques in grinding process for enhanced machinability: a review, J. Braz. Soc. Mech. Sci. Eng. 46 (2024) 199, https://doi.org/10.1007/s40430-024-04801-5.

[23] B.S. Linke, Sustainability concerns in the life cycle of bonded grinding tools, CIRP J. Manuf. Sci. Technol. 7 (2014) 258–263, https://doi.org/10.1016/j.cirpj.2014.05.002.

[24] A. Basem, M. Naji, H.A. Al-Asadi, M. Sediq Safi, G. Daminova, M. Alhadrawi, M. J. Alfaker, S. Islam, Small-quantity cooling lubrication in creep-feed grinding: surface quality and residual stress analysis, Results Eng. 22 (2024) 102348, https://doi.org/10.1016/j.rineng.2024.102348.

[25] J. Ma, E. Cui, B. Zha, G. Zheng, K. Li, X. Cheng, L. Gu, Experimental assessment of cryogenic LN2 enhanced GNPs-Cu/ZrO2 multiphase composite nano-fluids MQL in the turning of GH4169, Mater. Today Commun. 48 (2025) 113321, https://doi.org/10.1016/J.MTCOMM.2025.113321.

[26] M. Danish, M.K. Gupta, S. Rubaiee, A. Ahmed, M.E. Korkmaz, Influence of hybrid Cryo-MQL lubri-cooling strategy on the machining and tribological characteristics of Inconel 718, Tribol. Int 163 (2021) 107178, https://doi.org/10.1016/J.TRIBOINT.2021.107178.

[27] E. Benedicto, D. Carou, E.M. Rubio, Technical, economic and environmental review of the lubrication/cooling systems used in machining processes, Procedia Eng. 184 (2017) 99–116, https://doi.org/10.1016/J.PROENG.2017.04.075.

[28] A.M. Khan, S. Anwar, M. Jamil, M.M. Nasr, M.K. Gupta, M. Saleh, S. Ahmad, M. Mia, Energy, environmental, economic, and technological analysis of Al-GnP Nanofluid- and cryogenic LN2-assisted sustainable machining of Ti-6Al-4V alloy, Metals 11 (2021) 88, https://doi.org/10.3390/MET11010088.

[29] H.N. Li, D. Axinte, Textured grinding wheels: a review, Int J. Mach. Tools Manuf. 109 (2016) 8–35, https://doi.org/10.1016/J.IJMACHTOOLS.2016.07.001.

[30] S. Costa, M. Pereira, J. Ribeiro, D. Soares, Texturing methods of abrasive grinding wheels: a systematic review, Materials 15 (2022) 8044, https://doi.org/10.3390/ma15228044.

[31] R. Peng, X. Chen, M. Zhou, L. Zhao, J. Gao, Process optimization via synergistic hBN/SiC nanofluid and internal cooling for low-damage grinding of Inconel 718, Ceram. Int. (2025), https://doi.org/10.1016/J.CERAMINT.2025.07.083.

[32] X. Zhang, Z. Zhou, D. Wen, Z. Shi, X. Chen, X. Tang, W. Rong, T. He, Grinding performance of MgF2 ceramics using biomimetic shark fin grinding wheels with different structure parameters, Ceram. Int. 50 (2024) 40943–40954, https://doi.org/10.1016/J.CERAMINT.2024.07.407.

[33] D. Wen, L. Wan, X. Zhang, T. He, Z. Chen, A.M.M. Ibrahim, Wear characteristics of diamond grinding wheels with biomimetic structures in grinding silicon carbide ceramics, Mater. Today Commun. 44 (2025) 112071, https://doi.org/10.1016/J.MTCOMM.2025.112071.

[34] S.B. Thekkoot Surendran, V.S. Sooraj, Sweating type surface grinding wheels for self-adaptable lubricant delivery governed by cutting temperature and speed, J. Manuf. Process 134 (2025) 915–931, https://doi.org/10.1016/J.JMAPRO.2024.12.081.

[35] S.D. Mihić, S. Cioc, I.D. Marinescu, M.C. Weismiller, Detailed study of fluid flow and heat transfer in the abrasive grinding contact using computational fluid dynamics methods, J. Manuf. Sci. Eng. 135 (2013) 041002, https://doi.org/10.1115/1.4023719.

[36] L. Zhao, R. Peng, J. Gao, Y. Li, M. Chen, Mechanistic design of porous self-lubricating grinding wheels with integrated internal cooling: role of PMMA and nickel-coated MoS_2 composites in machining enhancement, J. Mater. Process Technol. 340 (2025) 118877, https://doi.org/10.1016/J.JMATPROTEC.2025.118877.

[37] L. Zhao, R. Peng, J. Gao, Y. Li, X. Tang, X. Chen, Z. Tan, Synergistic nanofluids-porous self-lubricating internal cooling wheel for superalloy grinding, Int J. Mech. Sci. 302 (2025) 110576, https://doi.org/10.1016/J.IJMECSCI.2025.110576.

[38] J. Sieniawski, K. Nadolny, The effect upon grinding fluid demand and workpiece quality when an innovative zonal centrifugal provision method is implemented in the surface grinding of steel CrV12, J. Clean. Prod. 113 (2016) 960–972, https://doi.org/10.1016/J.JCLEPRO.2015.11.017.

[39] J. Sieniawski, K. Nadolny, Experimental study into the grinding force in surface grinding of steel CrV12 utilizing a zonal centrifugal coolant provision system, Proc. Inst. Mech. Eng. B J. Eng. Manuf. 232 (2016) 394–403, https://doi.org/10.1177/0954405416645256.

[40] T. Karpiński, J. Sieniawski, 2005, Cylindrical grinding wheel and a mold for its preparation, 203295.

[41] M. Barmouz, B. Azarhoushang, A. Zahedi, F. Rabiei, F. Steinhäuser, Progress in grinding performance by additive manufacturing of grinding wheels integrated with internal venturi cooling channels and surface slots, J. Manuf. Process 99 (2023) 485–500, https://doi.org/10.1016/J.JMAPRO.2023.05.078.

[42] K. Nadolny, Small-dimensional sandwich grinding wheels with a centrifugal coolant provision system for traverse internal cylindrical grinding of steel 100Cr6, J. Clean. Prod. 93 (2015) 354–363, https://doi.org/10.1016/J.JCLEPRO.2015.01.046.
[43] S. Costa, P. Capela, A. Hassui, J. Ribeiro, M. Pereira, D. Soares, CFD analysis of multi-layer cooling channels in three-dimensionally structured grinding wheels, Appl. Therm. Eng. 279 (2025) 127633, https://doi.org/10.1016/j.applthermaleng.2025.127633.
[44] R. Peng, W. Yan, L. Zhao, M. Chen, X. Xiao, Design and performance evaluation of a directional internal-cooling grooved grinding wheel with optimized coolant supply structure, J. Manuf. Process 141 (2025) 155–168, https://doi.org/10.1016/J.JMAPRO.2025.02.059.
[45] H. Yu, W. Zhang, Y. Lyu, J. Wang, Research on grinding forces of a bionic engineered grinding wheel, J. Manuf. Process 48 (2019) 185–190, https://doi.org/10.1016/J.JMAPRO.2019.10.031.
[46] C. Tian, Y. Wan, X. Li, Y. Rong, Permeability design and assessment of the additively manufactured metal-bonded diamond grinding wheel based on TPMS structures, Int J. Refract Met. Hard Mater. 114 (2023) 106237, https://doi.org/10.1016/J.IJRMHM.2023.106237.
[47] S.B. Thekkoot Surendran, V.S. Sooraj, Enhancing useful flow of cutting fluid and thermal performance in surface grinding via segmented wheel, Mater. Today Proc. 90 (2023) 208–213, https://doi.org/10.1016/J.MATPR.2023.06.090.
[48] Z. Wang, J. Li, Q. Liu, L. Chen, J. Lv, T. Yu, J. Zhao, No-impact trajectory design and fabrication of surface structured CBN grinding wheel by laser cladding remelting method, Opt. Laser Technol. 181 (2025) 111956, https://doi.org/10.1016/J.OPTLASTEC.2024.111956.
[49] H. Yu, K. Sun, W. Ren, J. Zhang, Z. Han, Synergistic improvement of grinding fluid utilization and workpiece surface quality using combinatorial bionic structured grinding wheels, J. Manuf. Process 130 (2024) 102–117, https://doi.org/10.1016/J.JMAPRO.2024.08.046.
[50] M. Hong, G. Huang, H. Fan, L. Wu, W. Li, Y. Xu, X. Xu, W. Zeng, Investigation of additive-manufactured spiral textured grinding wheel (TGW) for grinding of zirconia ceramics, Ceram. Int. 51 (2025) 35448–35462, https://doi.org/10.1016/J.CERAMINT.2025.05.266.
[51] C. Baumgart, J.J. Radziwill, F. Kuster, K. Wegener, A study of the interaction between coolant jet nozzle flow and the airflow around a grinding wheel in cylindrical grinding, Procedia CIRP 58 (2017) 517–522, https://doi.org/10.1016/J.PROCIR.2017.03.261.
[52] S. Costa, P. Capela, M.S. Souza, J.R. Gomes, L. Carvalho, M. Pereira, D. Soares, A new grinding wheel design with a 3D internal cooling structure system, J. Manuf. Mater. Process. 8 (2024) 159, https://doi.org/10.3390/jmmp8040159.
[53] A. Reid, R. Rossi, C. Cottini, A. Benassi, CFD simulation of a Rushton turbine stirred-tank using open-source software with critical evaluation of MRF-based rotation modeling, Meccanica 60 (2025) 1613–1637, https://doi.org/10.1007/s11012-024-01824-z.
[54] M. Saeedipour, S. Vincent, J.L. Estivalezes, Toward a fully resolved volume of fluid simulation of the phase inversion problem, Acta Mech. 232 (2021) 2695–2714, https://doi.org/10.1007/S00707-021-02972-Z/FIGURES/21.
[55] J. Chen, Y. Fu, N. Qian, C.Y. Ching, D. Ewing, Q. He, A study on thermal performance of revolving heat pipe grinding wheel, Appl. Therm. Eng. 182 (2021) 116065, https://doi.org/10.1016/J.APPLTHERMALENG.2020.116065.
[56] J. Kundrák, A.P. Markopoulos, N.E. Karkalos, Numerical simulation of grinding with realistic representation of grinding wheel and workpiece movements: a finite volumes study, Procedia CIRP 58 (2017) 275–280, https://doi.org/10.1016/J.PROCIR.2017.03.192.
[57] A. Gupta, P. Swami, A.S.S. Balan, P. Kuppan, R. Oyyaravelu, Numerical modeling and heat transfer analysis of minimum quantity lubrication grinding of inconel 751, Mater. Today Proc. 5 (2018) 13358–13366, https://doi.org/10.1016/J.MATPR.2018.02.328.
[58] S. Mirjalili, A. Mani, A conservative second order phase field model for simulation of N-phase flows, J. Comput. Phys. 498 (2024) 112657, https://doi.org/10.1016/J.JCP.2023.112657.
[59] S.B. Pope, 2000, Turbulent flows, (2000). https://doi.org/10.1017/CBO9780511840531.
[60] J.C. Lasheras, E.J. Hopfinger, Liquid jet instability and atomization in a coaxial gas stream, Annu Rev. Fluid Mech. 32 (2000) 275–308, https://doi.org/10.1146/ANNUREV.FLUID.32.1.275/CITE/REFWORKS.
[61] H. Yu, W. Zhang, S. Zhang, J. Zhang, Z. Han, Optimization of hydrodynamic properties of structured grinding wheels based on combinatorial bionics, Tribol. Int. 173 (2022) 107651, https://doi.org/10.1016/J.TRIBOINT.2022.107651.
[62] S. Costa, A. Souza, L. Neves, J. Ribeiro, M. Pereira, D. Soares, Coolant flow in structured grinding wheels: CFD validation via high-speed imaging and particle tracking, Appl. Therm. Eng. 281 (2025) 128689, https://doi.org/10.1016/j.applthermaleng.2025.128689.
[63] S. Costa, P. Capela, A. Hassui, J. Ribeiro, M. Pereira, D. Soares, Performance of 3D-structured grinding wheels with multi-layer internal cooling channels, Results Eng. 28 (2025) 107881, https://doi.org/10.1016/j.rineng.2025.107881.
[64] S. Malkin, C. Guo. Grinding technology: theory and application of machining with abrasives, 2nd ed., Industrial Press Inc, New York, 2008.
[65] X. Chen, W.B. Rowe, Analysis and simulation of the grinding process. Part I: generation of the grinding wheel surface, Int. J. Mach. Tools Manuf. 36 (1996) 871–882, https://doi.org/10.1016/0890-6955(96)00116-2.
[66] B. Denkena, J. Köhler, J. Kästner, Chip formation in grinding: an experimental study, Prod. Eng. 6 (2012) 107–115, https://doi.org/10.1007/S11740-011-0360-8/FIGURES/10.
[67] E. Brinksmeier, A. Giwerzew, Chip formation mechanisms in grinding at low speeds, CIRP Ann. 52 (2003) 253–258, https://doi.org/10.1016/S0007-8506(07)60578-2.
[68] Z. Guo, B. Guo, Q. Zhao, Z. Zeng, L. Xu, Wear characteristics of micro-structured CVD diamond grinding tools, Wear (2023) 204569, https://doi.org/10.1016/J.WEAR.2022.204569, 514-515.
[69] P. Capela, S.F. Carvalho, S. Costa, S. Souza, M. Pereira, L. Carvalho, J.R. Gomes, D. Soares, Wear Behavior of Grinding Wheels With Superficial Cooling Channels, in: ASME International Mechanical Engineering Congress and Exposition, American Society of Mechanical Engineers, 2021 p. V003T03A034.